Published in final edited form as:
Neuroimage. 2012 February 15; 59(4): 3201–3211. doi:10.1016/j.neuroimage.2011.11.062.

Somatosensory activation of two fingers can be discriminated with ultrahigh-density diffuse optical tomography

Christina Habermehl[1], **Susanne Holtze**[2], **Jens Steinbrink**[1,3], **Stefan P. Koch**[1], **Hellmuth Obrig**[1,2,4], **Jan Mehnert**[1,2], and **Christoph H. Schmitz**[1,5]

[1]Berlin NeuroImaging Center, Charité Universitätsmedizin, Charitéplatz 1, 10117 Berlin, Germany

[2]Max Planck Institute for Human Cognitive and Brain Sciences, Stephanstr. 1a, 04103 Leipzig, Germany

[3]Center for Strokeresearch Berlin (CSB), Charité Universitätsmedizin, 10098 Berlin, Germany

[4]Clinic for Cognitive Neurology, University Hospital Leipzig, Germany

[5]NIRx Medizintechnik GmbH, Baumbachstr. 17, 13189 Berlin, Germany

Abstract

Topographic non-invasive near infrared spectroscopy (NIRS) has become a well-established tool for functional brain imaging. Applying up to 100 optodes over the head of a subject, allows achieving a spatial resolution in the centimeter range. This resolution is poor compared to other functional imaging tools.

However, recently it was shown that diffuse optical tomography (DOT) as an extension of NIRS based on high-density (HD) probe arrays and supplemented by an advanced image reconstruction procedure allows describing activation patterns with a spatial resolution in the millimeter range. Building on these findings, we hypothesize that HD-DOT may render very focal activations accessible which would be missed by the traditionally used sparse arrays. We examined activation patterns in the primary somato-sensory cortex, since its somatotopic organization is very fine-grained. We performed a vibrotactile stimulation study of the first and fifth finger in eight human subjects, using a 900-channel continuous-wave DOT imaging system for achieving a higher resolution than conventional topographic NIRS. To compare the results to a well established high-resolution imaging technique, the same paradigm was investigated in the same subjects by means of functional magnetic resonance imaging (fMRI). In this work, we tested the advantage of ultrahigh-density probe arrays and show that highly focal activations would be missed by classical next-nearest neighbor NIRS-approach, but also by DOT, when using a sparse probe array. Distinct activation patterns for both fingers correlated well with the expected neuro-anatomy in five of eight subjects. Additionally we show that activation for different fingers are projected to different tissue depths in the DOT image. Comparison to the fMRI data yielded similar activation foci in seven out of ten finger representations in these five subjects when comparing the lateral localization of DOT and fMRI results.

Corresponding Author: Christina Habermehl, Charité Berlin, Klinik f. Neurologie, BNIC, Charitéplatz 1, D-10117 Berlin, phone: +49 30 450 560 019, fax: +49 30 450 560 936, christina.habermehl@charite.de.

Keywords

near infrared spectroscopy; NIRS; diffuse optical tomography; DOT; high-density diffuse optical tomography human; brain; somatotopy; vibrotactile stimulation; comparison NIRS fMRI; multimodal imaging

1. Introduction

NIRS is an established method to measure cortical activation noninvasively. The usually practiced *topographic* approach relies on next-nearest neighbor source-detector combinations with a sparse array of optical fibers. Commonly, NIRS studies use inter-optode distances between 2 and 4 cm, covering particular regions of interest (Franceschini et al., 2003; Holper et al., 2010) or the whole head (Franceschini et al., 2006; Takeuchi et al., 2009), depending on the imaging device, the number of available optodes and the field of study.

Topographic NIRS has been widely used within the last decade, and has become an accepted tool in brain research. The method is known for having a good temporal and sufficient spatial resolution. The fields of application are wide and range from physiological (Holper et al., 2009; Miyai et al., 2001) to psychological (Hyde et al., 2010; Nakahachi et al., 2010; Wartenburger et al., 2007) and psychiatric studies (Kameyama et al., 2006; Zhu et al., 2010). Previously, resting state analysis using NIRS with a high coverage of the head identified the same functional connectivity networks as fMRI experiments (Franceschini et al., 2006; Mesquita et al., 2010). Promising, though still at the beginning of development, is the application of NIRS in brain-computer-interfaces (BCI) where, additionally to the use of electrophysiological signals in BCIs, researchers focus on hemodynamic signals that can be measured with NIRS (Fazli et al., 2012; Sitaram et al., 2009).

Applications of NIRS mainly focus on hemodynamic changes during task performance. However, there are promising clinical applications of NIRS such as the quantification of cerebral oxygenation and perfusion (Habermehl et al., 2011; Highton et al., 2010; Mittnacht, 2010) provided the confounding effects of extracerebral hemodynamic signals from tissue like the scalp can be accounted for. Although most of the applications are in an experimental stage and used only in research, NIRS has the potential to become a bedside monitoring tool in clinical routine and neurorehabilitation.

Beside the sensitivity to superficial signals, the spatial resolution of NIRS in its topographic approach is limited to several centimeters. A better resolution may not be required for many applications, but for clinical applications higher spatial resolution and depth discrimination are mandatory.

For example, investigation of rehabilitation induced changes of cortical function and neuroplasticity need a higher spatial resolution than conventional topographic NIRS can provide. Unfortunately, NIRS provides only functional patterns but no anatomical information. Individual anatomic structures are however often needed, especially in cases where there is a high inter-subject variability concerning the location and characteristics of activation due to specific tasks or stimulations.

A higher spatial resolution can be provided by using the multi-distance approach (Barbour et al., 2001; Bluestone et al., 2001), which uses dense fiber arrays to yield measurements from multiple source-detector distances and combinations. The approach of diffuse optical tomography (DOT) aims at transforming the signal content from different measuring

distances into depth information, thus forming three-dimensional image maps instead of the planar back projection obtained with topographic NIRS. In the following sections we will refer only to the topographic approach using next-nearest neighbor source-detector (SD) distances as 'NIRS.' The tomographic approach using multiple SD distances will be denoted, 'DOT'. In contrast to other groups, e.g.(Zeff et al., 2007) that use fiber grids with a minimum SD separation of 13 mm and fibers that are separated sources and detectors (not co-located) we applied a tighter fiber arrangement (see Methods section), exceeding the sampling density of other multi-distance approaches. In the following, we refer to this strategy as ultrahigh-density DOT.

In DOT, image reconstruction of hemodynamic changes consists of two main steps. First, the forward model of light propagation in tissue is calculated with assumed optical properties in the medium. Second, the inverse problem of recovering interior optical properties from measured surface data is solved. Image reconstruction is an ill-posed and under-determined problem and many research groups have focused on one or both parts of the problem (Arridge and Hebden, 1997; Arridge and Schweiger, 1997; Boas et al., 2002; Dehghani et al., 2008; Dehghani et al., 2009; Fang, 2010; Fang and Boas, 2009; Gibson and Dehghani, 2009; Gibson et al., 2005; Xu et al., 2005).

Light propagation in tissue is usually described by solving the diffusion equation on a finite element (FE) mesh or by modeling the photon transport in the tissue with a Monte Carlo (MC) simulation. For both methods, different tools have been developed by various groups. The free available NIRFAST software (Dehghani et al., 2008) provides a toolbox to calculate forward models based on the FE method with different mesh geometries and the possibility to incorporate individually generated meshes of different tissue types like breast and head models. Other free tools that are available include fast, voxel based MC simulations for photon transport using graphics processing units based parallel computing techniques (Fang and Boas, 2009) and another one to solve MC simulations based on FE meshes (Fang, 2010). In this study we used the commercial NAVI software (NIRx Medical Technology LLC, Glen Head, NY, USA).

The calculation of the forward model leads to a sensitivity or weight matrix that contains information about the contributions of each voxel of the investigated medium to the measured surface data. Generally speaking, the image of internal optical properties can be regarded the product of the inverted weight matrix with the measured surface data.

Three-dimensional DOT of human brain function has not been widely used so far. Published studies have focused on motor (Boas et al., 2004; Gibson et al., 2006; Joseph et al., 2006) and visual stimulation (White and Culver, 2010a; Zeff et al., 2007). Boas et al. (2004) first demonstrated 3D reconstructed DOT images of motor activation in the human cortex and compared these to topographic backprojection maps. The group demonstrated an increasing lateral resolution, when overlapping multi-distance measurements were used. Moreover, (White and Culver, 2010b) compared different optical fiber layouts and showed a significantly improved lateral resolution with a dense imaging grid compared to sparser grids.

In this study, we show that for demanding functional mapping tasks, such as demonstrated on the somatosensory system, not only does DOT in conjunction with high spatial sampling improve spatial resolution, but that is essential to visualize and distinguish the activation patterns. In contrast to many studies focusing the primary motor-system (Boas et al., 2004; Franceschini et al., 2003; Joseph et al., 2006) or primary/secondary visual system (Liao et al., 2010; White and Culver, 2010a; Zeff et al., 2007), we are only aware of two reports on somatosensory studies with NIRS (Custo et al., 2010; Franceschini et al., 2003), both using a

median nerve stimulation procedure. Thus, it seems to be an issue to resolve a more delicate somatosensory cortical activation with the classical topographic approach.

The primary somatosensory cortex (SI) was chosen here as a model system for several reasons: The superficial location at the posterior wall of the central sulcus makes it easily accessible to DOT measurements. Activations within SI are of small extent with short distances between representational areas of the fingers of one hand, suitable to demonstrate the need for and the benefit of high spatially resolved optical imaging. Furthermore, the highly individual and variable representational distribution provides a challenge and an interesting quality assessment for the comparison between NIRS and fMRI activations. And finally, beyond pure and basic research, there may be relevant future clinical applications in neurorehabilitation and rehabilitation monitoring, e.g. in stroke patients by assessing cortical neuronal plasticity.

In previous fMRI studies, finger representations have been confirmed to be localized within the contralateral postcentral gyrus and to show a somatotopic arrangement; generally, the first finger (thumb, d1) is represented in the most lateral, anterior and inferior position, with the other finger representations following in a superior medial direction along the central sulcus (Maldjian et al. 1999; Kurth et al. 2000; Weibull et al. 2008). Repeated measurements show comparable results for individual subjects. However, there is high inter-individual variability in somatotopic arrangement as well as in hemodynamic response strength (Schweizer et al. 2008; Kurth et al. 2000).

In the present work, we extended our previously published results on vibrotactile finger stimulation (Koch et al., 2010) towards the comparison of classical topographic image generation and a three-dimensional image reconstruction. Additionally, the same subjects underwent fMRI using the same experimental design to compare the functional activations of both imaging modalities. Finally, the individual position of optical fibers in the forward model were taken into account in the current study allowing to co-register volumes of functional activation with the individual anatomy.

Optical topography is exceedingly used in brain research compared to optical tomography. In this work, we show that there are applications where a three-dimensional tomographic approach is essential to image brain activity: with a topographic setup or even with a conventionally dense tomographic setup the specific activation foci cannot be distinguished properly. Furthermore, we demonstrate that our imaging and reconstruction procedure is able to separate cortical answers to different stimuli not only laterally but also transversally, with the activation pattern being found in different tissue depths. Additionally, we show that DOT and 3T fMRI as tools of functional brain imaging in humans yield comparable results.

2. Methods

2.1 Subjects and Stimulus Procedure

We investigated eight healthy right-handed volunteers (mean age 26.8 ± 4.6 years, 2 female) who had no history of any neurological disease. Written consent was obtained from each volunteer prior to the experiment. Subjects were monetarily rewarded for their participation. The study was approved of by the local ethic committee.

Volunteers underwent vibrotactile stimulation of the 1st (thumb, d1) and 5th finger (little finger, d5) of their right hand using a piezoelectric transducer (model PL-127.251, PI Ceramic, Lederhose, Germany) with a flat semicircle-shaped rubber pad (diameter: 13 mm, Fig. 1a); the frequency of the vibration was 40 Hz. The transducer was gently fixed at the participant’s fingertips with adhesive tape to assure the correct position throughout the

experiment. D1 and d5 were stimulated 40 times each. Stimulation periods of 20 sec were separated by resting periods of equal length. The sequence of d1 and d5 stimulation was pseudo-randomized but identical for all subjects and for both the DOT and the fMRI sessions. For DOT measurement, the subjects sat in a chair in a dimly-lit, silent room. The fMRI measurement was performed in supine position. Except from the position, the stimulation procedure was identical for both, the DOT and the fMRI experiments. In addition to the fMRI measurements in a 3T scanner, which was performed on a subsequent day after the DOT measurements we acquired an anatomical MRI in a 1.5 T scanner just prior to the DOT session in each participant.

For each subject four data sets were acquired: (i) a 1.5T anatomical scan prior to (ii) the DOT measurement, (iii) a 3T functional and (iv) anatomical MRI measurement.

2.2 Optical Data Acquisition

We used a DYNOT 232 instrument (NIRx Medizintechnik GmbH, Berlin, Germany) to acquire the DOT data. The system performs continuous-wave measurements using two frequency-encoded laser sources at 760 nm and 830 nm with a sampling rate of 1.8Hz in a time-multiplexed scanning fashion. The instrument employs an optical switch to provide a large number of illumination sites in a sequential illumination fashion. In conjunction with dynamic gain switching of the optical detectors, this provides the very high dynamic measurement range needed for diffuse-tomographic multi-distance measurements. Details of the measuring system can be found elsewhere (Schmitz et al., 2002). In the present study DOT measurements used 30 fiber-optic probes (optodes). Each optode can act as a source and as a detector, thereby providing 900 combinations, each entering the analysis as one optical data channel. The optodes were arranged in a rectangular grid of 6 × 5 probe positions, with a center-to-center distance of 7.5 mm for neighboring optodes (see, Fig. 1b for schematic image). Because of the co-located source-detector design and the tight fiber arrangement, our setup allows for uniquely dense spatial sampling, from 0 cm source-detector distance (SDD) (i.e, co-located) to about 30 mm SDD. Because the spatial sampling density is much higher than in other tomographic or multi-distance approaches (e.g. minimum SD distance 19 mm: (Boas et al., 2004), 13 mm: (Zeff et al., 2007), (Gregg et al., 2010)), we refer to this strategy in this paper as ultrahigh-density DOT.

The instrument's rigid scaffolding head gear employs individual spring-loaded mounts of the fiber tips and allows parting of the subject’s hair. It provides a stable optical contact to the skin to minimize artifacts from mechanical instabilities or subject motion. Since the activation for finger stimulation is expected to be located over the left, postcentral gyrus, contralateral to the stimulated hand, we located the probe grid around the C3 position relating to the 10–20 System (Klem et al., 1999).

2.3 Co-registration of Probe Position and Anatomy

Co-registration of the individual optode-positions and the cortical anatomy required three steps.

First the optical probe positions on the subject’s head had to be projected to the correct positions of the forward problem solver’s geometry. To this end we acquired anatomical MRIs prior to the functional DOT-measurements in each participant (T1-weighted MPRAGE; TR=94 ms, TE=4 ms, flip angle 12°, voxel size 1 mm × 1 mm × 1 mm; 1.5 T, Magnetom Vision System; Siemens, Erlangen, Germany). To locate the probe grid fiduciary marks were used in the individual anatomical MRI: The four corners of our grid array were marked by Vitamin E capsules which give a clear contrast in T1 weighted MR images (Fig. 1c).

Next we co-registered the subject's anatomic scan (Fig. 1c) with the MR scan of the generic head model (Fig. 1d), on which our finite-element-mesh is based. This was done using the spatial normalization tool of SPM8 (Statistical Parametric Mapping; Wellcome Department for Cognitive Neurology, University College London, United Kingdom; www.fil.ion.ucl.ac.uk/spm/software/spm8; (Friston et al., 1995)). For this step, we defined the generic brain atlas as the template, and the individual MR scan served as the source image. SPM8 first computes an affine, and subsequently a non-linear transformation that warps the source image to the template without losing structural information (Ashburner et al., 2011). Fig. 1e shows an example of the transformed anatomy of a participant whose fiduciary marks were translocated to the finite element model space (FE-space).

Finally, we assigned the translocated positions of the fiducials to the FE mesh that we used to calculate the forward model (Fig. 1f). The positions of all 30 optodes on the FE model surface were interpolated between the fiducials.

2.4 Forward Model

To create the weight (Jacobian) matrix (**W**) we used the BrainModeler tool of the NIRx NAVI imaging suite, which is implemented in MATLAB (The MathWorks, Natick, MA, USA). The weight matrix contains information about the impact of each DOT voxel on the signals that are measured by all source-detector combinations on the surface of the medium:

$$\delta\mathbf{R}=\mathbf{W}\delta\mathbf{x},$$

where **R** is the vector containing the readings for all source-detector combinations, and **x** is the vector containing the optical property of interest (e.g., absorption coefficient) for all image voxels. In this linear perturbation approach it is assumed that small changes $\delta\mathbf{x_i}$ lead to proportional changes $\delta\mathbf{R_j}$.

Modeling the entire volume of the head would be computationally too demanding and would result in an overly large data set. Therefore the generic head model is subdivided into a library of overlapping finite element (FE) meshes, which can be selected according to the requirements of the experiment. The meshes are based on a single-subject brain atlas, obtained by an anatomical MR scan with 1 mm resolution (Fig. 1d). For each of these meshes there are approx. 400 boundary nodes on the head surface with a spatial resolution of 4 mm. These surface nodes are considered as potential source/detector positions and the FEM discretized photon diffusion equation using Type III boundary condition (Paulsen and Jiang, 1995) was solved for each submesh, providing the reference detector values and the weight function, respectively. The forward solution was computed based on the simplified assumption of homogenous interior optical properties (μ_a = 0.06 cm^{-1}, μ_s= 10 cm^{-1}).

We selected the sub-mesh that best approximated the area of our measurements, according to the translocated positions of the fiber grid (Fig. 1f). This sub-mesh was used for all subjects and contains 3884 nodes and 16772 tetrahedrons. Its dimension is 60 mm (thickness) × 71 mm (width) × 78 mm (height) (Fig. 1g). Because the fiber positions within the mesh varied between subjects, we individually assigned the positions of the optical fibers to the mesh for each participant.

2.5 Image Reconstruction and Statistics for DOT

2.5.1 Data Preprocessing and Quality—Raw data were band-pass filtered between 0.016 and 0.4 Hz to attenuate physiological noise (very slow fluctuations and pulse). Data channels exceeding a noise level of 15% (coefficient of variation) were excluded from further analysis. For seven of the eight participants all 900 data channels were retained for

image reconstruction. For the remaining participant (subject 5) 84 channels exceeded the noise level and were discarded, so that 816 channels were used for the image reconstruction. Due to the better fiber-skin contact in all other subjects, we observed inferior data quality in this subject, as judged by the variance of the raw data. We are aware that the threshold of 15% is a rather weak criterion allowing most of the channels to be used for reconstruction, but the main procedure defining 'activated DOTvoxels' is the t-test after image reconstruction (see below). It separates DOTvoxels showing real activation over a longer period after stimulus onset from those that fluctuates randomly.

When looking at different source-detector separations (e.g., 7.5 mm vs. 30 mm) we did observe deterioration of data quality with increasing distances but this was limited to few channels still not reaching the 15% level. Consistently we observed a slightly better signal-to-noise level in data measured with 760 nm (to which HbR contributes more).

2.5.2 Image reconstruction—We obtained images of hemodynamic changes using the normalized difference method (Pei et al., 2001b) in which differences between predicted and measured surface data are related to changes of interior optical properties (e.g. absorption) of the investigated medium compared to a reference medium (perturbation approach). Instead of recovering absolute values, which causes difficulties when an arbitrary target medium is imaged with diffuse light, the reconstruction procedure aims to reconstruct relative changes of interior optical properties and therefore uses relative detector readings.

One main limitation of perturbation methods is that they can produce incorrect solutions if the reference medium which is used to produce the initial guess differs considerably from the real background optical properties. Reconstructing relative changes rather than absolute values greatly relieves the demands on the accuracy of the initial guess (Pei et al., 2001a; Pei et al., 2001b).

By using the perturbation approach, the image reconstruction is reduced to an inversion problem of **W**. To make the weight matrix more uniform and less ill-conditioned, and to suppress numerical errors and accelerate convergence, **W** is scaled by normalizing the column vectors to their respective mean values. The inversion is then calculated by performing a truncated singular value decomposition using all singular values that explain 98% of the data.

2.5.3 Statistics—To identify DOTvoxels with a stimulus-related hemodynamic response, t-tests between a baseline interval from -10 to -1 s and the stimulus interval from 13 to 20 s both with regard to stimulus onset were calculated. A typical time course in an activated DOTvoxel with an increase in HbO and a decrease in HbR peaking some 5–7 s after stimulus onset, can be seen in supplementary figure 1a.

We here focus on changes in HbR, which we regard the more reliable indicator of a hemodynamic response in the brain's cortex. HbO is often confounded by superficial tissue signaling such as blood pressure (Franceschini et al., 2003) and other global (i.e., non-task specific) hemodynamics. Since the activation-induced increase in regional cerebral blood flow (rCBF) overcompensates the regional increase in oxygen uptake (Fox and Raichle, 1986) a decrease in HbR is expected. Negative T-values in the HbR maps therefore indicate activation in the respective DOTvoxel. In this study we evaluated activation data on single subject level. Due to the different signal amplitudes and signal-to-noise levels we did not use the same cutoff-value for all subjects and conditions, but determined individual thresholds. The T-values ranged between 70% and 90% of the maximum t-value. Only DOTvoxels with values below this threshold are displayed as 'active'.

The NAVI software provides the reconstructed images in a 2D array, which contains a time series of the whole experiment for each node of the FE mesh. All statistical calculations were performed on this 2D-array and then transformed into Cartesian 3D space using the griddata3 routine from MATLAB (version 9, The Mathworks, Natick, MA, USA).

Supplementary figure 1b shows one example of these result volumes from one subject before thresholding. Note that, due to the preceding co-registration of the subject's anatomical MR and the FE model, the reconstructed volume is located in the correct spatial orientation with respect to the participant's individual anatomy.

2.6 Topographic and sparse tomographic analysis

We sought to test the hypothesis that tomographic imaging renders a better and more adequate representation of the activation pattern in the somatosensory cortex. To allow a direct comparison of a topographic, a sparse tomographic and a dense tomographic approach in the same data sets, we defined a subset of second nearest neighbor (2NN) source detector combinations mimicking a topographic approach (Fig. 3, first row for setup and results). This topographic approach was based on five sources and four detectors which were not co-located. Similar to the tomographic approach, data were band pass filtered at 0.016–0.4 Hz. To compute concentration changes in HbO and HbR we used a modified Beer-Lambert law as is usually done in topographic approaches (Cope et al., 1988). Statistical inference was based on the same approach as for the tomographic imaging: t-tests between pre-stimulus baseline to late-stimulation intervals (−13 to −1 s and 13 to 20 s with respect to stimulus onset).

To further assess the influence of probe density on the separability between activation foci we additionally mimicked a sparser sampling DOT approach, using 15 instead of 30 probes and 225 optical data channels instead of 900 (Fig. 3, second row). The image reconstruction for this sparse tomographic approach was the same as described in section 2.5.

2.7 Functional MRI Data Acquisition and Analysis

To provide a 'gold standard' of spatial resolution with regard to the hemodynamic response we acquired functional MRIs in the volunteers. The stimulation procedure was identical to the DOT experiment. FMRI data were acquired on a 3T MR scanner (TRIO, Siemens, Erlangen Germany) employing a T2*-weighted BOLD-sensitive echoplanar imaging (EPI) sequence (TR=2000 ms, TE=18 ms, 3 mm isotropic fMRIvoxel size) covering almost the entire brain. Immediately before functional imaging, an anatomical image volume was acquired (TR 1300 ms TE 3.93 ms, flip angle 10°, 1 mm isotropic fMRIvoxel size) for superposition of statistical t-maps. For each subject, we acquired 1200 fMR scans, resulting in a total duration of 54 min. SPM8 was used to perform standard analysis on imaging data. The initial ten images of each data set were discarded to account for T1 saturation effects. Preprocessing of functional images comprised realignment to the mean functional image and spatial smoothing (Gaussian kernel; FWHM=6 mm × 6 mm × 6 mm). Voxelwise time courses were temporally high-pass-filtered (cutoff period 128 s). Statistical t-maps were calculated by regression analysis based on the general linear model (Friston et al., 1995), defining regressor functions as the respective stimulus onset functions convolved with the canonical hemodynamic response function. According to the procedure applied to the DOT data, we set individual thresholds for all subjects and conditions in the fMRI experiment. The resulting t-maps for both conditions were superimposed on the 1.5 T individual anatomical brain scans of each single subject, which were co-registered to the 3T anatomical brain scans. Data were masked within a hypothesis-driven region of interest (ROI) by selecting only clusters contralateral to stimulated hand. Thresholded t-maps of the two

conditions were then superimposed on the individual brain, which was extracted with the SPM8 segmentation tool.

3. Results

3.1 Ultrahigh-density DOT reveals distinct activations for 1st and 5th finger

In five (out of eight) subjects, we found two distinct separate activation foci for the two fingers using the ultrahigh-density DOT approach as shown in Fig. 2. The volumes were reconstructed from the 900 optical data channels and are mapped onto the individuals' anatomies. In these five participants, the activations projected to the post-central gyrus, in line with the expected activation in response to the vibrotactile stimulation. However, the exact locations of the activations for the two fingers are quite variable between individuals. Two subject (s4 & s6) showed the expected spatial orientation in the z-dimension with d1 activation inferior to d5 (s4) or with d1 activation anterior to d5 (s6).Three subjects (s2, s3 and s5) showed a pattern in which d1 stimulation elicited an activation superior to that during d5 stimulation. Although the individual functional-anatomical tomography was variable, the distance between activations of the d1 and d5 was quite homogeneous (mean distance $d_{(d1,d5)}$ 13.7 mm, standard deviation 5.6 mm).

The remaining 3 participants (s1, s7 and s8) showed activation patterns for one of the two fingers only, when relying on the DOT measurements. It is noteworthy that the same subjects did not reveal two activation foci during the fMRI experiment, either (data not shown). Fig. 2 shows all volumes in which remarkable changes were detected for both, d1 (magenta) and d5 (blue) stimulation. To reach distinct non-overlapping areas of activation for each finger the thresholds were adjusted individually. A fixed threshold across subject blurred the contrast between fingers. This is demonstrated in supplementary figure 2. Thresholding at a fixed change of HbR (decrease with T-values < -2.5) substantially changed the results. This is unsurprising given the fact that absolute changes depend on many factors such as background optical properties which are known to vary largely between individuals and individual signal-to-noise ratio. The thresholding at a fixed percentage of the peak activation, however, yielded largely similar results as the arbitrary (hypothesis driven) threshold. We conclude that identifying small activations as can be expected in our paradigm (Ruben et al., 2001; Sanchez-Panchuelo et al., 2010) may require hypothesis-driven thresholds to identify distinct activation patterns.

3.2 Ultrahigh-density DOT is essential to identify small activations

To illustrate the relevance of ultrahigh-density DOT when small activation foci are targeted, we mimicked the results for approaches using sparser probe arrays. The results in two subjects (s2 and s6) are illustrated in Fig. 3. A sparse NIRS setup using a next neighbor approach with 12 channels (five sources and four detectors) is shown in the top row of Fig. 3. The middle row illustrates the results which would be obtained using a moderately dense sensor placement for tomography (15 fibers with all potential combinations), yielding 225 optical channels. For s2 (middle column), the differences between the results using the topographic NIRS approach (upper row) and those when using our here described ultrahigh-density array substantially differ while the intermediate dense tomography approach yields less distinct but principally similar activation foci. For s6 (right column), we can see a comparable orientation of the activation clusters with d1 anterior to d5 in all three setups, however T-value the activation foci in response to the different fingers are separated only when the ultrahigh-density approach is used.

While individual results differed in the other subjects the general superiority of the ultrahigh-density approach with regard to a separation of the activation foci was present in all data sets.

3.3 Ultrahigh-density DOT shows good relative depth resolution but the activation volumes are projected to extracerebral layers

One of the challenges in DOT is the correct depth localization because the underlying reconstruction methods favor solutions close to the tissue surface and therefore have a tendency to underestimate activation depth. This effect is particularly prominent in partial-view DOT imaging such as the backreflection geometry that is necessary in optical neuroimaging. To illustrate the effect, Fig. 4a shows two activation clusters in a frontal view. The activation areas are clearly separated, with the d1 representation located somewhat deeper than that of the d5. This clearly demonstrates the ability of ultrahigh-density DOT to resolve neuroactivation with good spatial resolution not only laterally, but also with remarkable relative depth discrimination.

While both activations are resolved in depth, the overlay with the anatomical structure demonstrates that the absolute depth placement is incorrect; both activation regions are projected to structural areas outside of the cortex. The reconstruction algorithm manages to locate the activations some distance below the outermost tissue layers but fails to achieve a more accurate placement within the brain matter. This is a well-known phenomenon which is caused mainly by the fact that the weight matrix W derived from the forward model has the highest sensitivity values close to the surface and a significant decrease in deeper layers. As a result, any solution to the inverse problem that includes superficial optical changes is heavily favoured over deeper-laying variations in optical dynamics. There are several strategies to counter this effect (Niu et al., 2010; Xu et al., 2007), each of which with particular advantages and disadvantages. The problem is to find objective criteria for manipulating W prior to the image reconstruction (Niu, Tian et al. 2010) or to adjust the reconstructed images to the correct depth. The method by Xu, Graber et al. has not been tested on physiological data so far. In our study we used a physiology/anatomy driven approach to correct the depth localization of the reconstructed volumes. Instead of applying model-based correction schemes, which bear significant risk of image distortion in themselves, we affine-transformed the DOT result and this way forced it into the cortical layers (Fig. 4 b, c). Based on the knowledge that somatosensory finger representation is mainly found in superficial cortical areas, we determined the minimum distance that was needed to project the result volumes “back” into the outermost cortical layer. Relating to the outer boundaries of the activation foci, it was consistently found that a translocation of about 15 mm parallel to the head surface was needed to place the activation in cortical tissue. This was the least assumptive and invasive correction strategy and it led to a conservation of the size and relative orientation of the activation clusters to each other. No lateral distortions of the activation clusters were observed due to this affine transformation.

3.4 DOT and fMRI find comparable lateral positions in seven out of ten finger representations

Fig. 5 illustrates the comparison between the results of DOT when compared to the corresponding fMRI measurements. Two clearly separate foci of activation for the d1 and d5 stimulation were seen - with both methods - in five of the eight subjects (s2–s6) The left column shows the reconstructed DOT results, and the right column contains the fMRI findings, all mapped onto the individual anatomies of the subjects.

Table 1 presents the coordinates of centers of activation for both fingers and imaging modalities. These coordinates were determined by normalizing all anatomical scans and the

result volumes from both, the DOT and fMRI experiment, to a standard brain (Evans et al., 1993) using SPM 8. The Euclidean distances between DOT and fMRI activation were calculated for each condition and subject for the lateral distance $d_{DOT(x,y),\ fMR(Ix,y)}$ and the distance in 3D space $d_{DOT(x,y,z),fMRI(x,y,z)}$. Regarding the absolute position of the activation foci we find six out of ten finger representations where the position error between DOT and fMRI result is less than 10 mm in 3D space (lateral and depth difference) and in seven out of ten finger representations when taking only the lateral distance into account. When viewing the distances of the x,y- coordinates one should keep in mind, that there is still some positioning error occurring from the previously described depth localization problem in DOT which not only affects the z-direction but also the x-direction.

From our view more interesting than the absolute position of the activation is the relative orientation of the foci towards each other: three out of the five subjects (s2 – s4, top three rows) show substantially similar activation patterns in DOT and fMRI. Interestingly, while s4 displays the typically assumed functional organization that places d1 activation inferior to d5, s2 and s3 show the opposite behavior, and consistently do so in both DOT and fMRI. Reconstructing this “switched” and rather unusual activation pattern with both methods give further indication that ultrahigh-density DOT and fMRI have a comparable access to cortical activation. In two other subjects (s5 & s6) the pattern was not identical, with a more posterior rather than inferior orientation of d5 (s5) and with a higher distance of both activations in s6 in fMRI and DOT. In these two cases, only the activation for d1 was comparably localized.

4. Discussion

The aim of the current multi-modal functional imaging study was two-fold. Firstly, we wanted to show that ultrahigh-density DOT allows identifying distinct activation patterns for stimuli that are known to activate cortical areas of a small extend. Secondly, we investigated the comparability of high density optical measurements with the gold-standard in functional brain imaging, fMRI.

For the optical measurement, we used an ultrahigh-density grid of optical fibers with an inter-optode distance of less than 10 mm. We showed that a classic 12-channel topographic approach fails to resolve small activations and that a medium-dense grid can only partly reconstruct the expected results.

By attaching 30 optical fibers over an area of about 12 cm^2, we achieve a much denser spatial sampling compared to previous tomography approaches that use wider inter-optode distances (Custo et al., 2010; Dehghani et al., 2009; White and Culver, 2010a). We found that satisfactory results in terms of the location and separation of small functional activations such as present in the somatosensory system can only be achieved with DOT if the spatial sampling density approaches the scale on which feature resolution is desired, in our case, about 10 mm.

The benefit of ultrahigh-density DOT is further substantiated by the similarities between the findings in high-resolution DOT and fMRI results. Seven of ten finger representations were detected in the same location. In three out of five subjects, showing two activation foci, we found a similar relative orientation of the activation maps, including two unusual switched patterns. For three remaining subjects, a stimulus answer could be detected neither with DOT nor in fMRI, which we take as further indication that both imaging modalities provide comparable access to small activations.

Even though the activation patterns showed strong qualitative similarities in both methods, we also observed consistent differences worth mentioning. For almost every subject, we

received more than one result cluster below the chosen threshold for DOT, whereas in fMRI mostly one cluster for each stimulus was present. One possible explanation for this observation may be that methodological differences in the specifics of each of the modalities' analyses introduce this bias. Even though it is also possible that these additional clusters of activation in the DOT result could be false positive results, we deem this unlikely, given the fact that these areas appear in isolated places and in the form of continuous patterns, rather than showing a distributed, grainy appearance throughout the entire volume, as one would expect from noise. Even though we demonstrate the high functional sensitivity and good lateral resolution of ultrahigh-density DOT, there is significant potential in improving the depth profiling accuracy. Although we observe the remarkable capability of resolving different activation depths, the anatomical localization of those is still poor. The algorithm underestimates the activation depth and places the activation in superficial layers that correspond mostly to extracortical areas, such as the scalp and skull.

We have good reason to assume that the activation actually stems from the cortex. Recently we demonstrated that our imaging system using the same fiber configuration is able to access hemodynamics the cortex (Habermehl et al., 2011). Furthermore, the observed signals show distinct focal areas instead of noisy patterns that correspond well with the known idiosyncrasy of hemodynamics connected with functional activation of the brain (Obrig and Villringer, 2003). This is substantiated by the observed DOT signals, such as in supplementary figure 1a, which shows one block averaged time course (HbO, HbR, and HbT) of one DOTvoxel in an activated area of a single subject for stimulation of d1. Specifically, extracerebral hemodynamics from the scalp show different behavior and are dictated by global effects, such as blood pressure changes, and reaction to temperature, local pressure by the optodes, etc. Such extracerebral signals can still have a deteriorative effect on the measured functional activation because they origin from the outermost tissue layers and pose a much larger contribution to the measured signal than the functional activation. There have been described ways of correcting for these signal contributions (Gregg et al., 2010); however, we found such corrections not necessary for the ultrahigh-density DOT approach used in this work.

There are a number of methods to improve depth localization in DOT. Because this was not the scope of the present work, we did not explore those in detail, but would rather mention them. One approach to solve this problem is the manipulation of the weight matrix with constraining the result space to DOTvoxel that are located within cortical tissue. Other less constraining algorithms look to correct the position error introduced in the reconstruction process. One proposed method (Niu et al., 2010) adjusts the weight matrix by multiplying a matrix with an inversely arranged order of increasing values from outer to deeper layers, thus counterbalancing the loss of sensitivity in deeper layers. The problem with such correction methods is the identification of objective criteria to what extent and in which way to adjust the weight matrix. One way of dealing with this problem has been introduced by (Xu et al., 2007), in which a filter matrix is applied on the reconstructed images. This filter is derived by encoding every DOTvoxel location with a unique temporal signature and thus determining the contribution of all parts of the medium to the image voxel.

One main limitation of accuracy in the applied DOT method is the generic forward model geometry. The generation of individual forward models is time and energy consuming and not feasible when many subjects are investigated. It has been shown by (Custo et al., 2010) that using a generic head model can lead to an image reconstruction within the correct gyrus. The relative difference method, which we applied for image reconstruction (Pei et al., 2001b) has been proven to be robust to inaccuracies of the initial guess and therefore allowed us to use a forward model with homogenous interior properties. Nevertheless,

differences in the skull geometry of subject and forward model and high variability of cortical structures can lead to distortions of results. A comparison of different forward models with a weighting of accuracy and efficiency has to be subject to further investigations.

Despite the improvement in methods for DOT there seem to be difficulties that make the method yet unattractive to be widely used for studies in adults. Table 2 gives an overview over, to our knowledge, all studies using 3D cw- DOT and image reconstruction to visualize human brain function. Most studies deal with visual, motor or somatosensory tasks. Studies concerning the limitations of DOT application in human brains are not published so far. A relatively high noise level of the data compared to other imaging modalities and a limited penetration depth may constrain extensive use of DOT. Furthermore a higher coverage of larger parts of the head for a whole head tomography is needed for the method to become a serious alternative for fMRI. One possibility to increase the signal-to-noise ratio and to extend the field of application could be the use extrinsic contrast agents instead of intrinsic agents like hemoglobin.

5. Conclusions

In this study we showed that ultrahigh-density DOT leads to a significant increase in the lateral resolution and allows distinguishing activation maps of two discrete fingers in a somatotopic stimulation task. We showed that a typical topographic approach cannot resolve these activations and even DOT with a medium-dense grid does not lead to satisfying results. With a fiducial mark approach we correlated DOT results and the subjects' neuroanatomy for a mapping of three-dimensional result clusters onto individual brain structures. The results were in good agreement with the known somatotopic finger arrangement, though showing a high inter-subject variability. Furthermore we demonstrated that DOT and fMRI reveal comparable results in difficult tasks with small activations. This is encouraging for further investigations aiming to promote high-density DOT as a potential monitoring tool in clinic and neurorehabilitation.

Highlights

- ultrahigh-density DOT has superior resolution compared to classical NIRS
- highly focal activations can be missed by classical NIRS and conventional DOT,
- comparison of ultrahigh-density DOT and fMRI data showed similar results in seven out of ten cases

Supplementary Material

Refer to Web version on PubMed Central for supplementary material.

Acknowledgments

This work was supported in part under NIH Grant Nos. R42NS050007 and R44NS049734 and by the National Bernstein Network Computational Neuroscience, Bernstein Focus: Neurotechnology, No. 01GQ0850, Project B3.

References

Arridge SR, Hebden JC. Optical imaging in medicine: II. Modelling and reconstruction. Phys Med Biol. 1997; 42:841–853. [PubMed: 9172263]

Arridge SR, Schweiger M. Image reconstruction in optical tomography. Philos Trans R Soc Lond B Biol Sci. 1997; 352:717–726. [PubMed: 9232860]

Ashburner, J.; Barnes, G.; Chen, C.; Daunizeau, J.; Flandin, G.; Friston, K.; Gitelman, D.; Kiebel, S.; Kilner, J.; Litvak, V.; Moran, R.; Penny, W.; Stephan, K.; Gitelman, D.; Henson, R.; Hutton, C.; Glauche, V.; Mattout, J.; Phillips, C. SPM8 Manual. London, UK: 2011.

Barbour RL, Graber HL, Pei Y, Zhong S, Schmitz CH. Optical tomographic imaging of dynamic features of dense-scattering media. J Opt Soc Am A Opt Image Sci Vis. 2001; 18:3018–3036. [PubMed: 11760200]

Bluestone A, Abdoulaev G, Schmitz C, Barbour R, Hielscher A. Three-dimensional optical tomography of hemodynamics in the human head. Opt Express. 2001; 9:272–286. [PubMed: 19421298]

Boas D, Culver J, Stott J, Dunn A. Three dimensional Monte Carlo code for photon migration through complex heterogeneous media including the adult human head. Opt Express. 2002; 10:159–170. [PubMed: 19424345]

Boas DA, Chen K, Grebert D, Franceschini MA. Improving the diffuse optical imaging spatial resolution of the cerebral hemodynamic response to brain activation in humans. Opt Lett. 2004; 29:1506–1508. [PubMed: 15259728]

Cope M, Delpy DT, Reynolds EO, Wray S, Wyatt J, van der Zee P. Methods of quantitating cerebral near infrared spectroscopy data. Adv Exp Med Biol. 1988; 222:183–189. [PubMed: 3129910]

Custo A, Boas DA, Tsuzuki D, Dan I, Mesquita R, Fischl B, Grimson WE, Wells W 3rd. Anatomical atlas-guided diffuse optical tomography of brain activation. Neuroimage. 2010; 49:561–567. [PubMed: 19643185]

Dehghani H, Eames ME, Yalavarthy PK, Davis SC, Srinivasan S, Carpenter CM, Pogue BW, Paulsen KD. Near infrared optical tomography using NIRFAST: Algorithm for numerical model and image reconstruction. Commun Numer Methods Eng. 2008; 25:711–732. [PubMed: 20182646]

Dehghani H, White BR, Zeff BW, Tizzard A, Culver JP. Depth sensitivity and image reconstruction analysis of dense imaging arrays for mapping brain function with diffuse optical tomography. Appl Opt. 2009; 48:D137–D143. [PubMed: 19340101]

Evans, AC.; Collins, DL.; Mills, SR.; Brown, ED.; Kelly, RL.; Peters, TM. 3D statistical neuroanatomical models from 305 MRI volumes; Proc. IEEE-Nuclear Science Symposium and Medical Imaging Conference; 1993. p. 1813-1817.

Fang Q. Mesh-based Monte Carlo method using fast ray-tracing in Plucker coordinates. Biomed Opt Express. 2010; 1:165–175. [PubMed: 21170299]

Fang Q, Boas DA. Monte Carlo simulation of photon migration in 3D turbid media accelerated by graphics processing units. Opt Express. 2009; 17:20178–20190. [PubMed: 19997242]

Fazli S, Mehnert J, Steinbrink J, Curio G, Villringer A, Muller KR, Blankertz B. Enhanced performance by a hybrid NIRS-EEG brain computer interface. Neuroimage. 2012; 59:519–529. [PubMed: 21840399]

Fox PT, Raichle ME. Focal physiological uncoupling of cerebral blood flow and oxidative metabolism during somatosensory stimulation in human subjects. Proc Natl Acad Sci U S A. 1986; 83:1140–1144. [PubMed: 3485282]

Franceschini MA, Fantini S, Thompson JH, Culver JP, Boas DA. Hemodynamic evoked response of the sensorimotor cortex measured noninvasively with near-infrared optical imaging. Psychophysiology. 2003; 40:548–560. [PubMed: 14570163]

Franceschini MA, Joseph DK, Huppert TJ, Diamond SG, Boas DA. Diffuse optical imaging of the whole head. J Biomed Opt. 2006; 11 054007.

Friston KJ, Holmes AP, Poline JB, Grasby PJ, Williams SC, Frackowiak RS, Turner R. Analysis of fMRI time-series revisited. Neuroimage. 1995; 2:45–53. [PubMed: 9343589]

Gibson A, Dehghani H. Diffuse optical imaging. Philos Transact A Math Phys Eng Sci. 2009; 367:3055–3072. [PubMed: 19581255]

Gibson AP, Austin T, Everdell NL, Schweiger M, Arridge SR, Meek JH, Wyatt JS, Delpy DT, Hebden JC. Three-dimensional whole-head optical tomography of passive motor evoked responses in the neonate. Neuroimage. 2006; 30:521–528. [PubMed: 16246586]

Gibson AP, Hebden JC, Arridge SR. Recent advances in diffuse optical imaging. Phys Med Biol. 2005; 50:R1–R43. [PubMed: 15773619]

Gregg NM, White BR, Zeff BW, Berger AJ, Culver JP. Brain specificity of diffuse optical imaging: improvements from superficial signal regression and tomography. Front Neuroenergetics. 2010:2.

Habermehl C, Schmitz CH, Steinbrink J. Contrast enhanced high-resolution diffuse optical tomography of the human brain using ICG. Opt Express. 2011; 19:18636–18644. [PubMed: 21935232]

Highton D, Elwell C, Smith M. Noninvasive cerebral oximetry: is there light at the end of the tunnel? Curr Opin Anaesthesiol. 2010; 23:576–581. [PubMed: 20830845]

Holper L, Biallas M, Wolf M. Task complexity relates to activation of cortical motor areas during uni- and bimanual performance: a functional NIRS study. Neuroimage. 2009; 46:1105–1113. [PubMed: 19306929]

Holper L, Muehlemann T, Scholkmann F, Eng K, Kiper D, Wolf M. Testing the potential of a virtual reality neurorehabilitation system during performance of observation, imagery and imitation of motor actions recorded by wireless functional near-infrared spectroscopy (fNIRS). J Neuroeng Rehabil. 2010; 7:57. [PubMed: 21122154]

Hyde DC, Boas DA, Blair C, Carey S. Near-infrared spectroscopy shows right parietal specialization for number in pre-verbal infants. Neuroimage. 2010; 53:647–652. [PubMed: 20561591]

Joseph DK, Huppert TJ, Franceschini MA, Boas DA. Diffuse optical tomography system to image brain activation with improved spatial resolution and validation with functional magnetic resonance imaging. Appl Opt. 2006; 45:8142–8151. [PubMed: 17068557]

Kameyama M, Fukuda M, Yamagishi Y, Sato T, Uehara T, Ito M, Suto T, Mikuni M. Frontal lobe function in bipolar disorder: a multichannel near-infrared spectroscopy study. Neuroimage. 2006; 29:172–184. [PubMed: 16125979]

Klem GH, Luders HO, Jasper HH, Elger C. The ten-twenty electrode system of the International Federation. The International Federation of Clinical Neurophysiology. Electroencephalogr Clin Neurophysiol Suppl. 1999; 52:3–6.

Koch SP, Habermehl C, Mehnert J, Schmitz CH, Holtze S, Villringer A, Steinbrink J, Obrig H. High-resolution optical functional mapping of the human somatosensory cortex. Front Neuroenergetics. 2010; 2:12. [PubMed: 20616883]

Kurth R, Villringer K, Curio G, Wolf KJ, Krause T, Repenthin J, Schwiemann J, Deuchert M, Villringer A. fMRI shows multiple somatotopic digit representations in human primary somatosensory cortex. Neuroreport. 2000; 11:1487–1491. [PubMed: 10841363]

Liao SM, Gregg NM, White BR, Zeff BW, Bjerkaas KA, Inder TE, Culver JP. Neonatal hemodynamic response to visual cortex activity: high-density near-infrared spectroscopy study. J Biomed Opt. 2010; 15 026010.

Maldjian JA, Gottschalk A, Patel RS, Detre JA, Alsop DC. The sensory somatotopic map of the human hand demonstrated at 4 Tesla. Neuroimage. 1999; 10:55–62. [PubMed: 10385581]

Mesquita RC, Franceschini MA, Boas DA. Resting state functional connectivity of the whole head with near-infrared spectroscopy. Biomed Opt Express. 2010; 1:324–336. [PubMed: 21258470]

Mittnacht AJ. Near infrared spectroscopy in children at high risk of low perfusion. Curr Opin Anaesthesiol. 2010; 23:342–347. [PubMed: 20421789]

Miyai I, Tanabe HC, Sase I, Eda H, Oda I, Konishi I, Tsunazawa Y, Suzuki T, Yanagida T, Kubota K. Cortical mapping of gait in humans: a near-infrared spectroscopic topography study. Neuroimage. 2001; 14:1186–1192. [PubMed: 11697950]

Nakahachi T, Ishii R, Iwase M, Canuet L, Takahashi H, Kurimoto R, Ikezawa K, Azechi M, Kajimoto O, Takeda M. Frontal cortex activation associated with speeded processing of visuospatial working memory revealed by multichannel near-infrared spectroscopy during Advanced Trail Making Test performance. Behav Brain Res. 2010; 215:21–27. [PubMed: 20600348]

Niu H, Tian F, Lin ZJ, Liu H. Development of a compensation algorithm for accurate depth localization in diffuse optical tomography. Opt Lett. 2010; 35:429–431. [PubMed: 20125744]

Obrig H, Villringer A. Beyond the visible--imaging the human brain with light. J Cereb Blood Flow Metab. 2003; 23:1–18. [PubMed: 12500086]

Paulsen KD, Jiang H. Spatially varying optical property reconstruction using a finite element diffusion equation approximation. Med Phys. 1995; 22:691–701. [PubMed: 7565358]

Pei Y, Graber H, Barbour R. Normalized-constraint algorithm for minimizing inter-parameter crosstalk in DC optical tomography. Opt Express. 2001a; 9:97–109. [PubMed: 19421278]

Pei Y, Graber HL, Barbour RL. Influence of Systematic Errors in Reference States on Image Quality and on Stability of Derived Information for dc Optical Imaging. Appl Opt. 2001b; 40:5755–5769. [PubMed: 18364867]

Ruben J, Schwiemann J, Deuchert M, Meyer R, Krause T, Curio G, Villringer K, Kurth R, Villringer A. Somatotopic organization of human secondary somatosensory cortex. Cereb Cortex. 2001; 11:463–473. [PubMed: 11313298]

Sanchez-Panchuelo RM, Francis S, Bowtell R, Schluppeck D. Mapping human somatosensory cortex in individual subjects with 7T functional MRI. J Neurophysiol. 2010; 103:2544–2556. [PubMed: 20164393]

Schmitz CH, Löcker M, Lasker JM, Hielscher A, Barbour RL. Instrumentation for fast functional optical tomography. Review of Scientific Intruments. 2002; 73:429–439.

Schweizer R, Voit D, Frahm J. Finger representations in human primary somatosensory cortex as revealed by high-resolution functional MRI of tactile stimulation. Neuroimage. 2008; 42:28–35. [PubMed: 18550386]

Sitaram R, Caria A, Birbaumer N. Hemodynamic brain-computer interfaces for communication and rehabilitation. Neural Netw. 2009; 22:1320–1328. [PubMed: 19524399]

Takeuchi M, Hori E, Takamoto K, Tran AH, Satoru K, Ishikawa A, Ono T, Endo S, Nishijo H. Brain cortical mapping by simultaneous recording of functional near infrared spectroscopy and electroencephalograms from the whole brain during right median nerve stimulation. Brain Topogr. 2009; 22:197–214. [PubMed: 19705276]

Wartenburger I, Steinbrink J, Telkemeyer S, Friedrich M, Friederici AD, Obrig H. The processing of prosody: Evidence of interhemispheric specialization at the age of four. Neuroimage. 2007; 34:416–425. [PubMed: 17056277]

Weibull A, Bjorkman A, Hall H, Rosen B, Lundborg G, Svensson J. Optimizing the mapping of finger areas in primary somatosensory cortex using functional MRI. Magn Reson Imaging. 2008; 26:1342–1351. [PubMed: 18550314]

White BR, Culver JP. Phase-encoded retinotopy as an evaluation of diffuse optical neuroimaging. Neuroimage. 2010a; 49:568–577. [PubMed: 19631755]

White BR, Culver JP. Quantitative evaluation of high-density diffuse optical tomography: in vivo resolution and mapping performance. J Biomed Opt. 2010b; 15 026006.

Wylie GR, Graber HL, Voelbel GT, Kohl AD, DeLuca J, Pei Y, Xu Y, Barbour RL. Using co-variations in the Hb signal to detect visual activation: a near infrared spectroscopic imaging study. Neuroimage. 2009; 47:473–481. [PubMed: 19398013]

Xu Y, Graber HL, Barbour RL. Image correction algorithm for functional three-dimensional diffuse optical tomography brain imaging. Appl Opt. 2007; 46:1693–1704. [PubMed: 17356612]

Xu Y, Pei Y, Graber HL, Barbour RL. Image quality improvement via spatial deconvolution in optical tomography: time-series imaging. J Biomed Opt. 2005; 10 051701.

Zeff BW, White BR, Dehghani H, Schlaggar BL, Culver JP. Retinotopic mapping of adult human visual cortex with high-density diffuse optical tomography. Proc Natl Acad Sci U S A. 2007; 104:12169–12174. [PubMed: 17616584]

Zhu Y, Liu X, Wang H, Jiang T, Fang Y, Hu H, Wang G, Wang X, Liu Z, Zhang K. Reduced prefrontal activation during Tower of London in first-episode schizophrenia: a multi-channel near-infrared spectroscopy study. Neurosci Lett. 2010; 478:136–140. [PubMed: 20457217]

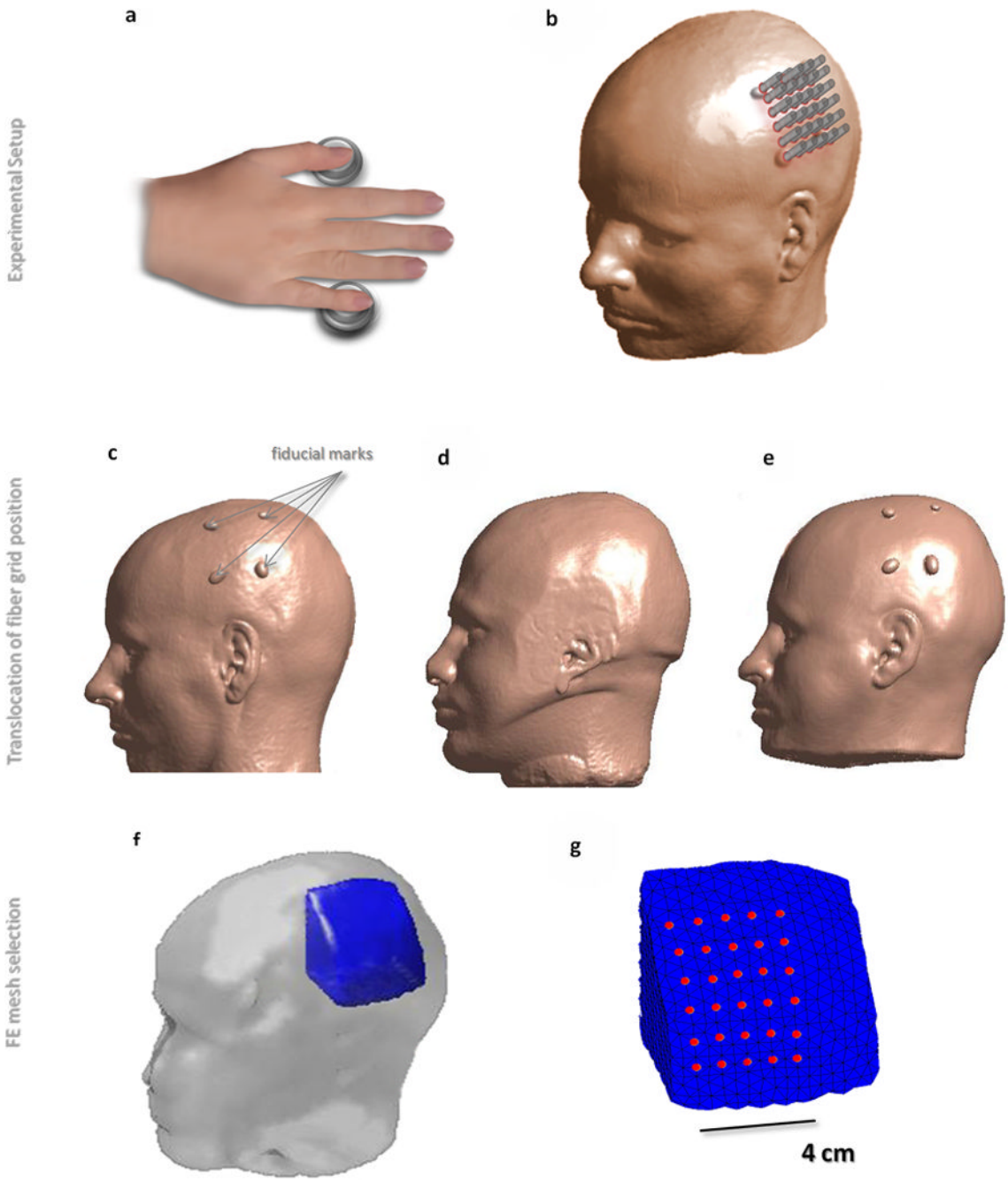

Fig. 1.

a) Experimental setup: The fingers d1 and d5 of the right hand were stimulated by piezoelectric vibration devices. b) 30 optical fibers (inter-optode distance 7.5 mm) were placed around C3. The positions of the fiber grid corners were marked with vitamin E capsules c) Fiduciary mark approach for co-registration: subject's MR scan in the real world space with the fiduciary marks on the head surface. d) Anatomic MR scan of the generic head atlas on which the FE mesh is based. e) Subject's MR scan, warped into space and shape of the atlas. f) Atlas with a sub-mesh (blue) of the FE model, covering the area of interest. g) Within the sub-mesh, the locations of the optical fibers (red dots) on the boundary were defined individually for each subject.

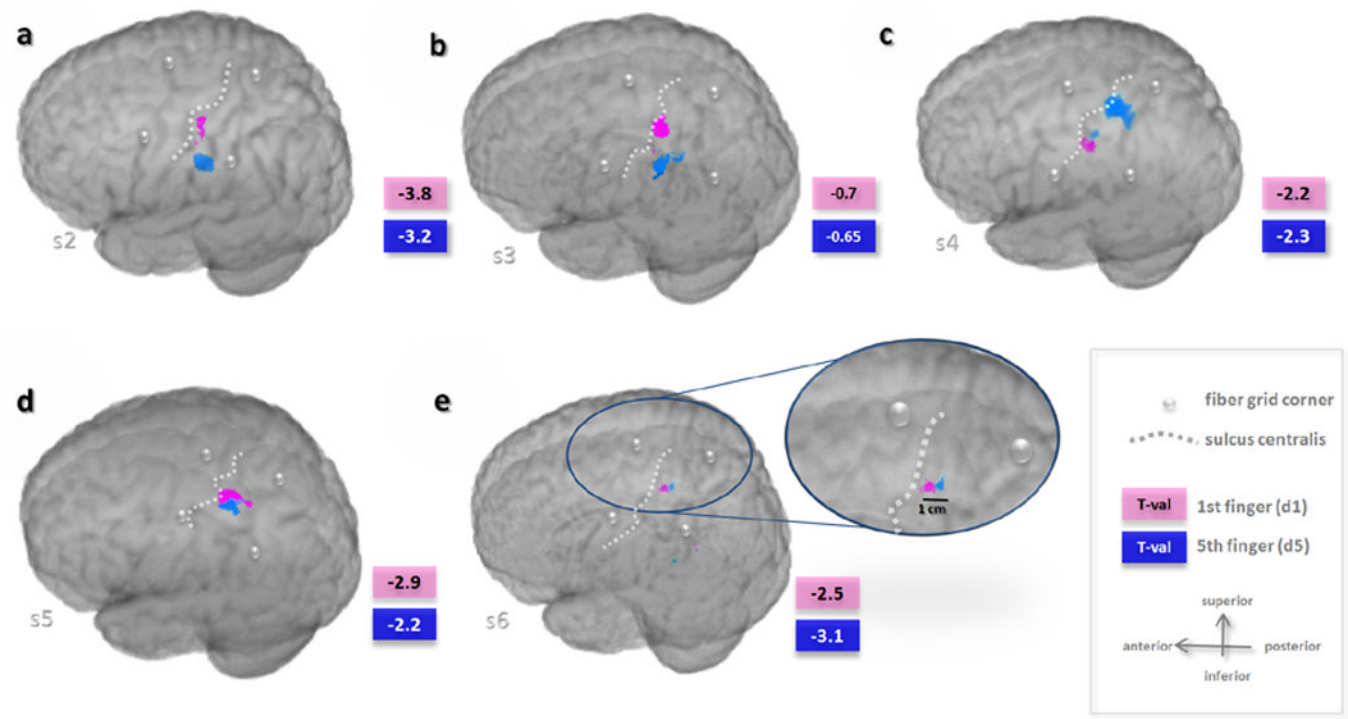

Fig. 2.

Results for vibrotactile stimulation of d1 (pink) and d5 (blue) of the right hand, mapped onto the individual brain anatomy of five subjects (s2–s6). Gray spheres indicate the edges of the grid. Gray dashed line: sulcus centralis. Colored boxes show the cut-off T-values for the different stimuli.

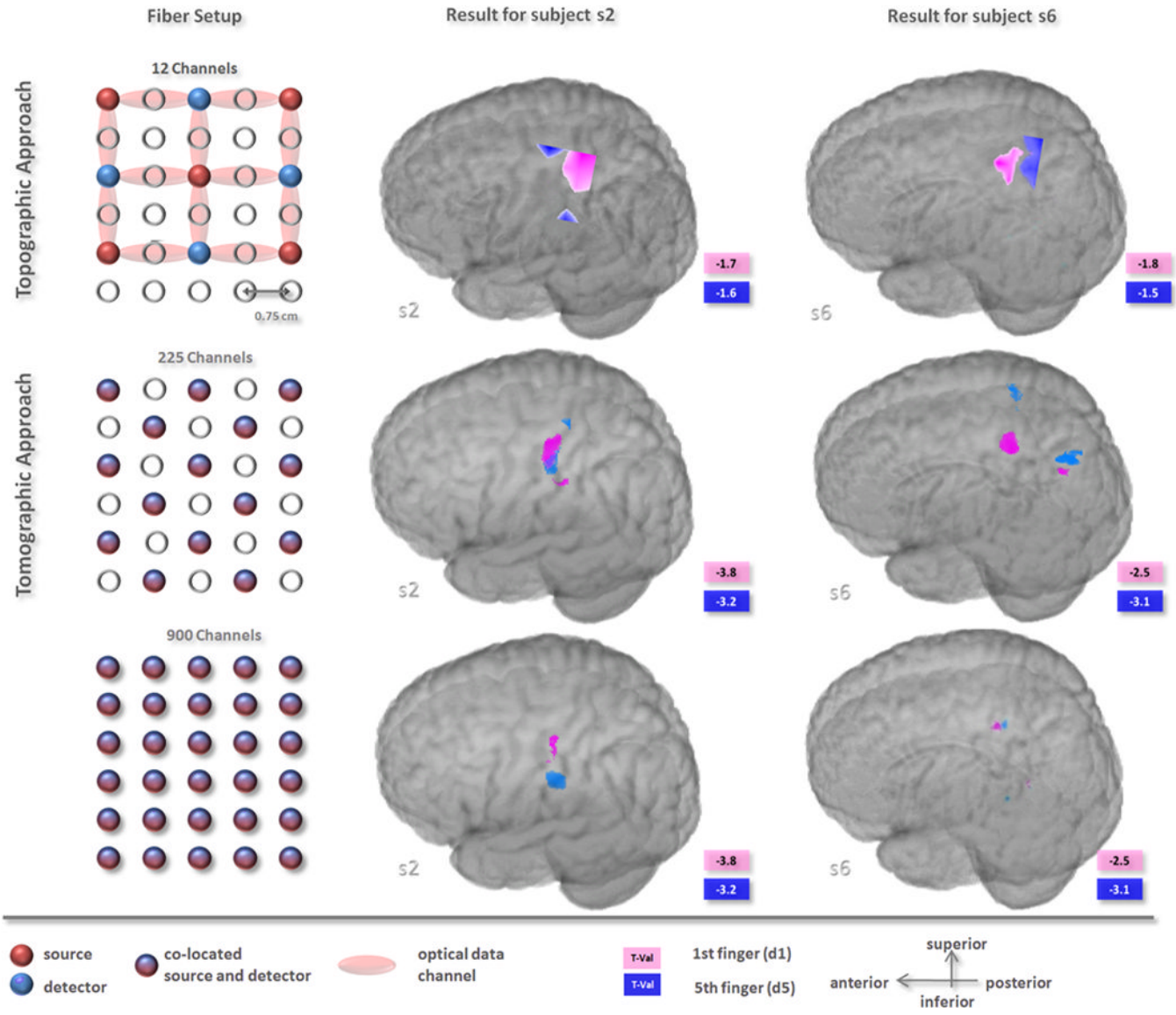

Fig. 3.

Comparison of activation patterns for vibrotactile stimulation of the d1 (pink) and d5 (blue) of the right hand for two subjects (s2, s6) when simulating three different densities of probes. Top row: To*p*ography approach using 12 NIRS- channels (light red ellipses between light source (red dots) and detectors (blue dots). Middle row: DOT approach with a medium-dense grid of co-located sources and detectors (bi-colored dots, minimum SD distance 15 mm) yields 225 optical data channels. Lower row: DOT approach with an ultrahigh-density grid and 900 channels. The increasing number of channels leads to a better lateral resolution and allows distinguishing between the two activations in both subjects (middle and right column).

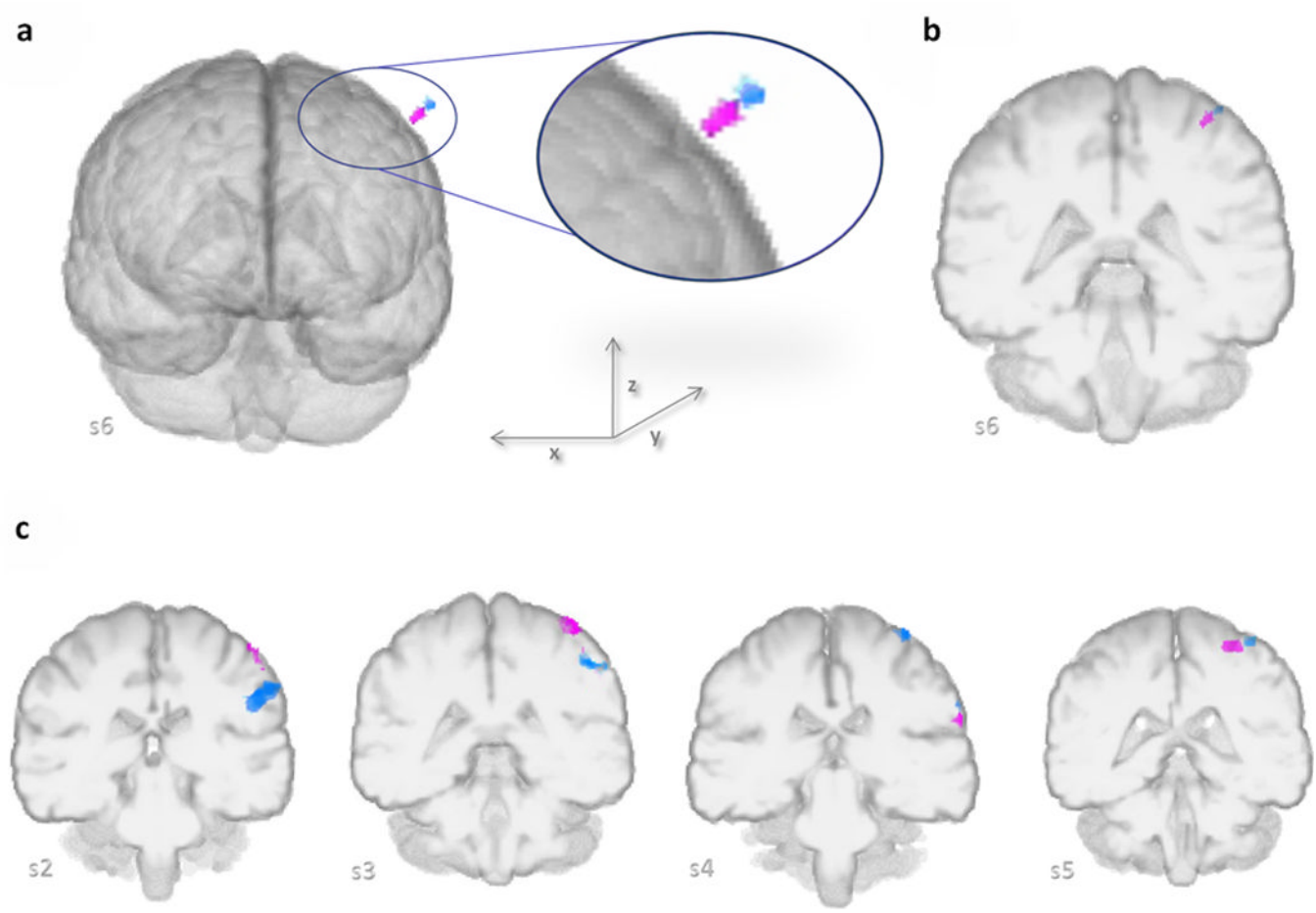

Fig. 4.

Reconstruction-based dislocation of the activation foci for d1 (pink) and d5 (blue) stimulation of the right hand in five subjects (s2–s6). a) Frontal view reveals that activation clusters for both fingers was determined in different tissue depths but still there is insufficient depth localization. b) Depth correction of the result volume localization: the volumes were translocated into the brain by 1.5 cm parallel to the head surface in x and z direction. c) Frontal view of a 1cm slice of the activated area for four subjects (s2–s5) after depth correction.

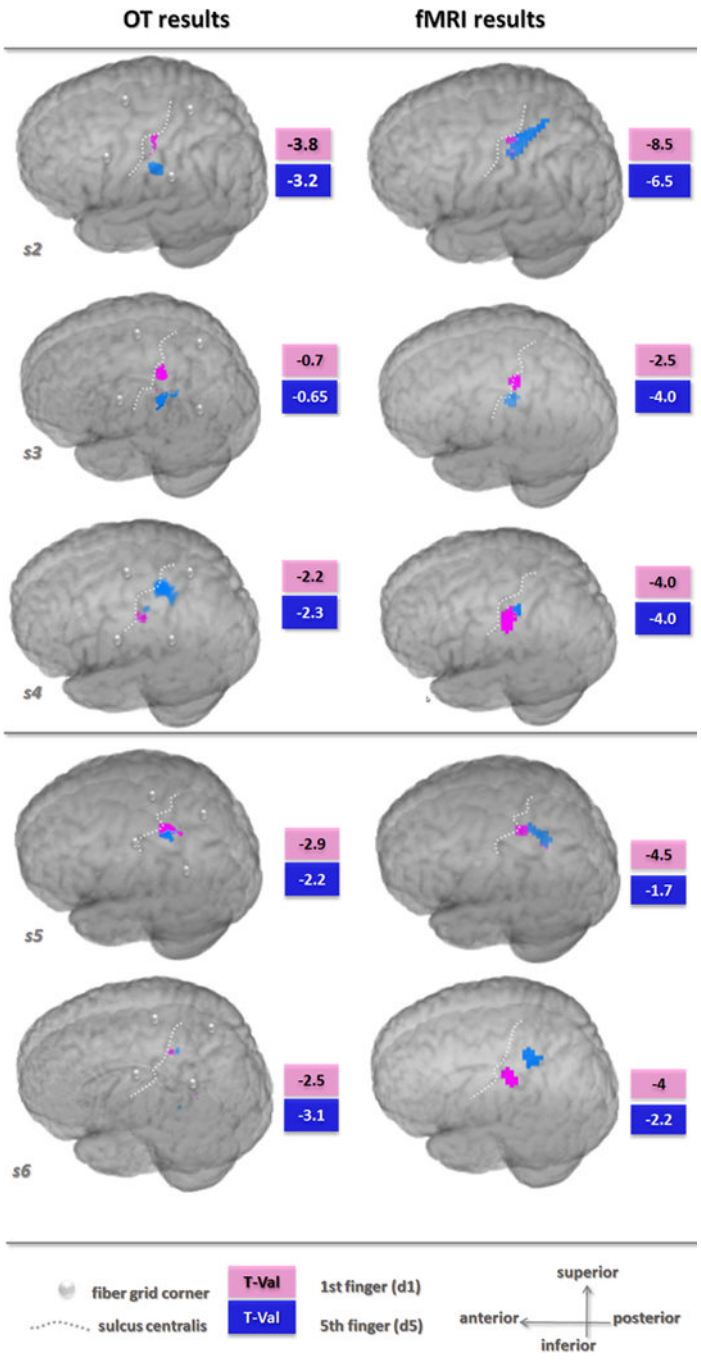

Fig. 5.

Comparison of NIRS and fMRI activation. All results were mapped onto the individual anatomy. Left column: reconstructed activation maps from DOT experiment for vibrotactile stimulation of d1 (pink) and d5 (blue) of the right hand for five subjects (s2–s6). Colored boxes indicate the cut-off T-values. Right column: results for the fMRI experiment.

Table 1

Coordinates of the centers of activation for DOT and fMRI. Euclidean distances d between the activation foci of both methods were calculated for $d(DOT_{x,y}, fMRI_{x,y})$ and $d(DOT_{x,y,z}, fMRI_{x,y,z})$

		DOT			fMRI				
Subject	**Finger**	**x**	**y**	**z**	**x**	**y**	**z**	**3D distance $d(DOT_{x,y,z}, fMRI_{x,y,z})$ [mm]**	**lateral distance $d(DOT_{x,y}, fMRI_{x,y})$ [mm]**
s2	***d1***	−50	−20	46	−56	−24	49	7.8	7.2
	d5	−56	−24	28	−55	−28	48	20.4	4.1
s3	***d1***	−40	−30	55	−56	−29	51	16.5	16.0
	d5	−51	−30	38	−59	−26	40	9.1	8.9
s4	***d1***	−64	−17	17	−66	−18	17	2.2	2.6
	d5	−62	−26	24	−59	−23	21	5.1	4.2
s5	***d1***	−31	−35	53	−49	−26	51	20.2	20.1
	d5	−40	−35	51	−42	−42	49	7.5	7.2
s6	***d1***	−38	−32	51	−50	−22	50	15.6	15.6
	d5	−41	−38	56	−48	−36	62	9.4	7.2

Table 2

Publications of DOT imaging experiments of human brain function.

Author	Neuroanatomical System	Neuroanatomical Correlation	Validation with fMRI
(Bluestone et al., 2001)	frontal (Valsalva)	no	no
(Boas et al., 2004)	motor	no	no
(Joseph et al., 2006)	motor	no	yes
(Zeff et al., 2007)	visual	no	no
(Wylie et al., 2009)	visual	no	no
(Custo et al., 2010)	somatosensory	yes	no
(White and Culver, 2010a)	visual	no	no
(White and Culver, 2010b)	visual	no	no
(Gregg et al., 2010)	visual	no	no
(Koch et al., 2010)	somatosensory	yes	no
this publication	*somatosensory*	*yes*	*yes*